Methods to design and evaluate transcranial ultrasonic lenses using acoustic holography

Diana Andrés, Alicia Carrión, Francisco Camarena, and Noé Jiménez*
Instituto de Instrumentación para Imagen Molecular (i3M), Universitat Politècnica de València, Consejo Superior de Investigaciones Científicas (CSIC), València, Spain

(Received 12 May 2023; revised 2 August 2023; accepted 22 September 2023; published 26 October 2023)

Ultrasonic three-dimensional printed holograms are getting increasing interest for transcranial therapies since they can correct skull aberrations and, simultaneously, adapt the acoustic field to particular brain targets. However, evaluating the targeting performance of these systems requires the measurement of complex volumetric acoustic fields, which in many practical situations cannot be estimated by direct hydrophone measurements. In this work, we apply single-plane holographic measurement techniques to experimentally calibrate and measure the full volumetric field produced by holographic lenses. Two *ex vivo* test cases are presented, a four-foci lens and a preclinical case, both targeting through a macaque skull for potential applications in blood–brain barrier opening (BBBO) studies. Time-reversal and angular spectrum projection methods are compared to direct experimental measurements. Results show that holographic projection methods can reconstruct the complex acoustic images produced by holographic lenses, matching direct measurements in all test cases. However, while direct measurements are restricted to transverse-field cross sections, holographic projection allows estimating the field on the whole targeting volume. In this way, the location and the full three-dimensional shape of all acoustic foci can be obtained. Furthermore, these techniques can provide the field at the surface of the lens to compare it to the design phase distribution. Using this procedure, complex volumetric acoustic fields can be reconstructed, saving significant measurement time and computational resources, and enabling an accurate characterization of phase plates and other holographic lens topologies.

DOI: 10.1103/PhysRevApplied.20.044071

I. INTRODUCTION

Holography was first proposed in optics at the midtwentieth century [1], and a short time later, around the 1960s, optical holography was combined with acoustic systems to generate optical images [2,3]. Acoustic holography allows imaging of optically opaque objects by combining diffraction and interference of acoustic wavefronts. Acoustic holographic imaging can use one or more acoustic beams to generate a sound field over an object. Then, the scattering is raster scanned to generate the image. In contrast, acousto-optical holographic techniques use the acoustic radiation pressure produced by the scattered field to generate an interference pattern at a liquid-gas interface, which is optically detected and used to generate a real-time image. In this context, several applications were already reviewed in the 1970s [4]. Later, Fourier-acoustics methods were applied in near-field acoustic holography techniques to evaluate the spatial pattern of vibration and radiation of acoustic sources [5,6], becoming a standard practice in acoustic engineering, e.g., for noise control and visualization, wave-field synthesis or loudspeaker design.

Recently, acoustic holography has become a powerful metrological tool for characterizing ultrasound fields generated by imaging and therapeutic applications, e.g., to characterize the radiation pattern produced by high-intensity focused ultrasound (HIFU) transducers [7,8]. This robust technique has been included as a part of IEC standards for ultrasound field metrology (IEC TS 62556:2014) [9]. Among other applications, holography has been proposed for acoustic field reconstruction through complex media [10]. In all these techniques, by measuring the acoustic field in a plane, e.g., transversally to an ultrasound beam, acoustic holography enables the knowledge of the field on an orthogonal plane, e.g., at the surface of the source.

Beyond these metrological and imaging techniques, holography has also been proposed to modulate acoustic wavefronts, generating acoustic images at a given target distance [11–14]. In this context, an acoustic image is defined as an acoustic field with arbitrary amplitude distribution. For ultrasound, phased-array systems were first proposed to tune the phase and amplitude along the surface of the transducer, mimicking a hologram, allowing to synthesize acoustic images even traversing absorbing areas [15]. While phased-arrays provide reconfigurability, the

*nojigon@upv.es

holographic information encoded on the transducer surface is strongly limited by the small number of piezoelectric elements of the current systems, limiting the hologram capability to generate complex acoustic images. With the rise of three-dimensional (3D) printing techniques, acoustic holograms can be generated via holographic lenses [16–19]. In this case, the holographic information becomes encoded in a passive structure, e.g., a 3D-printed lens of rough surface, which modulates the transmitted phase of the ultrasound field generated by a transducer. Among other applications, acoustic holograms have been proposed for ultrasound particle manipulation and trapping [20], acoustic vortex generation for transmitted [21] or reflected wavefronts [22], fast 3D printing via volumetric particle agglomeration [23], cell patterning [24], generation of cavitation patterns [25], producing arbitrary-shaped thermal patterns in tissues using ultrasound [26], tuning the acoustic field to control the total thermal dose on multiple targets for ultrasound hyperthermia [27], or performing 3D acoustic imaging using a single-channel transducer [28].

One emerging application of 3D-printed acoustic holograms is transcranial ultrasound for noninvasive brain therapy [29]. During transcranial ultrasound, the high acoustic contrast between soft-tissues and the skull bones produces strong beam refraction, scattering and absorption. For example, when using a single-element focused ultrasound transducer, the transmitted beam suffers from strong aberrations, and the targeting accuracy on the brain relies on simulation techniques during treatment planning to find the best-case scenario [30,31]. Therefore, wavefront aberration correction is desirable for precise targeting inside the brain [32,33]. To avoid these limitations, state-of-the-art clinical systems are based on therapeutic phased-array systems [34], allowing beam steering and aberration correction. However, in addition to their complexity and high cost, the steering range of therapeutic arrays is limited to a narrow region around the center of the array. Since they are composed of large piezoelectric surfaces, diffraction grating appears, limiting their focusing performance. Recently, 3D-printed holographic lenses coupled to flat or focused transducers have been proposed for aberration correction for focused beams [35], and even adapting the acoustic field to arbitrary brain targets [29,36]. It has been shown that acoustic holograms can generate arbitrary and complex patterns within human skulls [37]. They have been recently applied for blood–brain barrier opening in small laboratory animals, creating multiple sharply focused spots close to the diffraction limit [38], or wide focal areas [39]. In all these biomedical applications, a mandatory step before *in vivo* trials is to validate the acoustic field produced by the hologram in the relevant scenario.

Usually, the field generated by a therapeutic focused ultrasound transducer is assessed by direct measurements using hydrophones in a water tank [40]. While this approach is convenient for axisymmetric beams, e.g., those focusing at a single focal spot, the acoustic images produced by holographic lenses can present a far more complex spatial distribution over a large volume. In practice, the direct evaluation of the targeting performance of complex acoustic holograms requires a huge amount of data and measurement time, making unfeasible the estimation of the field over a large volume. In addition, for transcranial validation measurements, the size of the hydrophone limits the measurement range inside a skull. Faster techniques such as acousto-optical Fabry-Perot interferometers [41] require large sensors, limiting their application in transcranial ultrasound. Well-known optical methods such as schlieren imaging [42] or Doppler velocimetry [43] can provide a volumetric field estimation, but they require transparent optical windows and complex instrumentation. Note schlieren imaging can also be combined with optical holographic interferometers to estimate the acoustic field [44]. Indirect thermometric methods include the use of liquid-crystal thermochromic sheets sandwiched between sound-absorbing materials [45]. Ultrasound absorption results in heat, and the temperature change produces a variation of the optical color of the sheet, that is detected by a camera. This method results in a fast transverse-field scanning, however, it becomes difficult to calibrate. An alternative is the use of a thin sound-absorbing membrane combined with a thermal camera to measure the temperature at its surface [46]. However, the thermal radiation does not propagate through water and the method is limited to measurements on the surface of the water tank. To overcome these limitations, magnetic resonance thermometry techniques become more reliable for evaluating the field of acoustic holograms inside tissues [26], but these systems are expensive and unaffordable for many biomedical ultrasound research facilities. A faster and robust method is therefore desirable for volumetric field evaluation, in particular, for transcranial holographic devices.

In this work, we apply acoustic holography [7,8] to efficiently evaluate transcranial ultrasound fields produced by complex holographic lenses targeting through an *ex vivo* macaque skull. To evaluate the complex field produced by the lenses, three measurement methods are compared. First, direct hydrophone measurements, second, a projection technique based on time-reversal full-wave simulations and, third, a projection using the angular spectrum method. These methods are tested on two holographic lenses. The first one is designed to create four equidistant foci inside the macaque skull, while the second lens is designed to focus on the left postcommissural putamen of the specimen. Furthermore, the field at the exit surface of the lens is estimated experimentally using holographic techniques, and compared with the design phase field. The experimental fields are compared with full-wave simulations of the system, taken as the gold standard. Figure 1 illustrates the process to reconstruct the acoustic field at the focus from a single measured holographic plane. First,

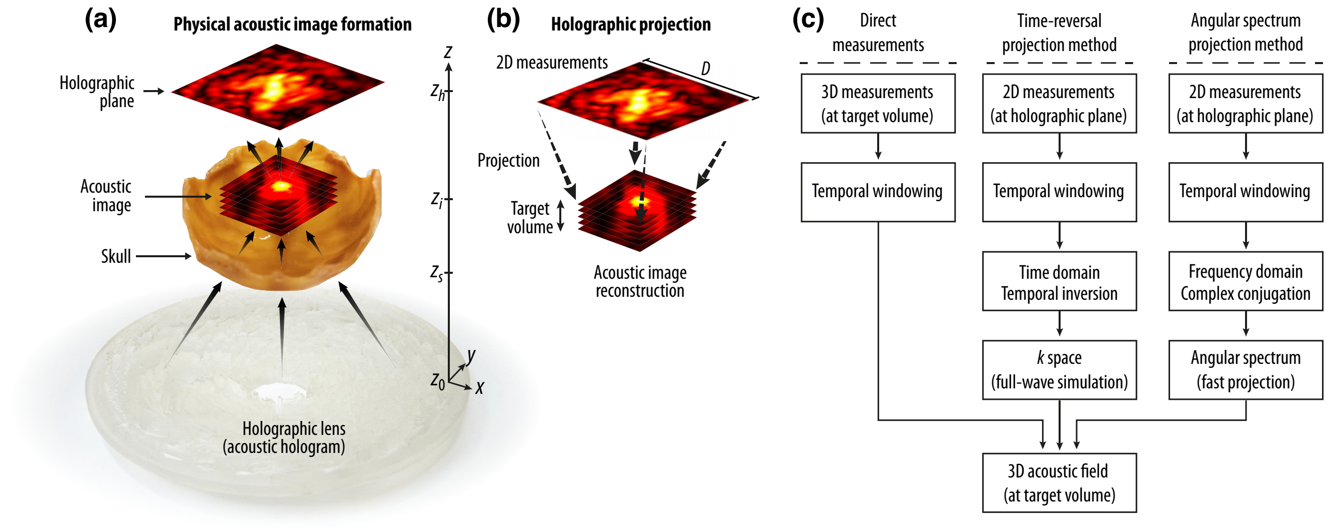

FIG. 1. (a) Schematic representation of the process to reconstruct the acoustic field at the focus from a single measured holographic plane. (b) Detail of the holographic projection. (c) Block diagram of the acoustic field reconstruction algorithms.

as shown in Fig. 1(a), a hologram modulates the wavefront generating an acoustic image inside a skull and the corresponding acoustic field in the holographic plane. Then, as shown in Fig. 1(b), a holographic projection technique is used to estimate the field along a target volume inside the skull. Figure 1(c) summarizes the three acoustic field reconstruction algorithms discussed in Sec. II.

II. TECHNIQUES FOR FIELD ESTIMATION

A. Direct measurements

Direct field measurements consist of scanning the area of interest with a hydrophone to record the corresponding waveforms. The hydrophone is usually mounted on a 3D positioning system and synchronized point-by-point measurements are performed to cover the desired target, e.g., two-dimensional (2D) planes or even 3D volumes. This technique presents the advantage that the acoustic pressure is directly measured. However, acquiring large volumes requires long measurement time and a large amount of data.

B. Holographic projection methods

To avoid point-to-point scanning over the whole volume, holographic projection methods only require the direct measurements at a plane, the holographic plane, normally transverse to the beam, located at a distance $z = z_h$ and covering a squared area of side length D (see Fig. 1). Then, the field at any point is calculated using a projection method.

1. Projection using time-reversal simulations

The time-reversal simulation projection method relies on the time-reversal invariance of the wave equation in a lossless medium. To project the field using time-reversal simulations, we use a full-wave simulation method, which solves the system of constitutive acoustic equations for a lossless homogeneous medium

$$\frac{\partial \rho(\mathbf{r},t)}{\partial t} = -\rho_0 \nabla \cdot \mathbf{v}(\mathbf{r},t) + \frac{\partial q(\mathbf{r}_h,t)}{\partial t}, \tag{1}$$

$$\frac{\partial \mathbf{v}(\mathbf{r},t)}{\partial t} = -\frac{1}{\rho_0}\nabla p(\mathbf{r},t), \tag{2}$$

$$p(\mathbf{r},t) = c_0^2 \rho(\mathbf{r},t), \tag{3}$$

where $\mathbf{v}(\mathbf{r},t)$ is the particle velocity field, $p(\mathbf{r},t)$ is the pressure, $\rho(\mathbf{r},t)$ is the acoustic density, ρ_0 is the medium density, c_0 is the sound speed, and $q(\mathbf{r}_h,t)$ is a spatial distribution of monopole sources, $\mathbf{r} = (x,y,z)$ and $\mathbf{r}_h = (x,y,z_h)$. These equations are solved numerically using a pseudospectral time-domain simulation method, implemented in the software k-Wave [47].

To make use of the time-reversal mirror symmetry, we acquire the experimental pressure waveforms over the holographic plane, $p_h(\mathbf{r}_h,t)$. A temporal window is applied to the signals to avoid reflections from boundaries. Then a temporal inversion is applied, letting $p_h(\mathbf{r}_h,t) \to p_h(\mathbf{r}_h,-t)$. Finally, the computational solution is found by setting the monopole source amplitude in Eq. (1) to $q(\mathbf{r}_h,t) = p_h(\mathbf{r}_h,-t)/c_0^2$. Note that time-reversal symmetry no longer holds in absorbing media [48]. In this work, we measure the field in pure water, whose absorption at ultrasonic frequencies can be considered negligible for a propagation path length of tens of wavelengths.

2. Projection using angular spectrum

Angular spectrum approach was also used to project the measured field at the holographic plane to several planes covering the target volume. This calculation was performed assuming neither absorption nor medium stratification. First, we calculate the frequency-domain amplitude of each spectral component of the field measured at the holographic plane, $z = z_h$, by a Fourier transform

$$P(x, y, z_h, \omega) = \int_{-\infty}^{\infty} p_h(\mathbf{r}_h, t)\, e^{i\omega t} dt. \tag{4}$$

Then, each spectral component of the field is complex conjugated, $P(x, y, z_h) \to P^*(x, y, z_h)$, to perform the temporal inversion in the frequency domain. In the spatial Fourier space, each spectral component of the field is given by

$$\tilde{P}^*\left(k_x, k_y, z_h\right) = \iint_{-\infty}^{+\infty} P^*(x, y, z_h) e^{i(k_x x + k_y y)} dx dy. \tag{5}$$

In this way, the field is decomposed into a spectrum of plane waves traveling in different directions, being their azimuth, θ, and elevation angles, ϕ, related to the transverse components of the wave vector by

$$k_x = k \cos\theta \sin\phi, \tag{6}$$

$$k_y = k \sin\theta \sin\phi, \tag{7}$$

where $k = \omega/c_0$. Each spectral component measured at the holographic plane $z = z_h$ is projected to the image plane $z = z_i$ by multiplying it in the Fourier space with the spectral propagator $H\left(k_x, k_y, z_i, z_h\right)$ as

$$\tilde{P}\left(k_x, k_y, z_i\right) = \tilde{P}\left(k_x, k_y, z_h\right) H\left(k_x, k_y, z_i, z_h\right), \tag{8}$$

where the spectral propagator for the pressure field, assuming a Fourier time convention of the type $e^{i\omega t}$, is defined as Liu and Waag [49],

$$H\left(k_x, k_y, z_i, z_h\right) = e^{-ik_z|z_h - z_i|}, \tag{9}$$

where the axial component of the wave vector is given by

$$k_z = \sqrt{k^2 - (k_x^2 + k_y^2)}. \tag{10}$$

Therefore, if $k_x^2 + k_y^2 \leq k^2$, then k_z is real and the propagator consists of propagating modes, while if $k_x^2 + k_y^2 > k^2$, then k_z is purely imaginary and the propagation function models the rapidly decaying evanescent modes of the field. Angular restriction is applied to avoid aliasing of rapidly oscillating waves propagating at grazing angles, using a low-pass circular window of radius $k_c = k\sqrt{D^2/2(D^2/2 + z^2)}$ in the k space [50].

For each spectral component, an inverse spatial Fourier transform of $\tilde{P}(k_x, k_y, z_i)$ is computed to recover the field amplitude $P(x, y, z_i)$ in the spatial domain,

$$P(x, y, z_i) = \iint_{-\infty}^{+\infty} \tilde{P}\left(k_x, k_y, z_i\right) e^{-i(k_x x + k_y y)} dx dy. \tag{11}$$

Finally, an inverse Fourier transform is applied at each location to recover the temporal waveforms in the time domain, as

$$p(\mathbf{r}_i, t) = \int_{-\infty}^{\infty} P(x, y, z_i)\, e^{-i\omega t} dt, \tag{12}$$

where $\mathbf{r}_i = (x, y, z_i)$. In this work, angular spectrum was used to evaluate the acoustic volume generated by the holographic lens inside the skull, $z_h > z > z_s$, z_s being the distance between the holographic plane and the inner surface of the skull. We project all spectral components of the measured signals.

Note, the Fourier-space product of Eq. (8) is equivalent to a spatial convolution from the plane z_h to z_i of the field $P^*(\mathbf{r}_h)$, given by Eq. (4), with the spectral propagator function, Eq. (9), in the spatial domain, the latter given by $h(\mathbf{r}_h, \mathbf{r}_i)$. In addition, the spatial domain propagator relates to Green's function of the Helmholtz equation in 3D as $h(\mathbf{r}_h, \mathbf{r}_i)/2 = \partial G(\mathbf{r}_i, \mathbf{r}_h)/\partial z$, where $G(\mathbf{r}_i, \mathbf{r}_h) = e^{-ikr}/4\pi r$, and $r = \sqrt{(x_i - x_h)^2 + (y_i - y_h)^2 + (z_i - z_h)^2}$. Therefore, Eq. (8) is equivalent to the second Rayleigh-Sommerfeld diffraction integral, but since the spectrums are calculated using the fast Fourier transform algorithm, it results in a more computationally efficient method.

III. EXPERIMENTAL SETUP

A. System design

A spherically focused custom-made ultrasound transducer with outer diameter OD = 100 mm and $R =$ 140 mm radius of curvature, with an inner aperture diameter of ID = 20 mm and central frequency $f = 500$ kHz was used. The piezoelectric ceramic is mounted in a customized stainless steel housing, with air backing. To tune the field of the transducer, a holographic 3D-printed lens was attached to it. Evaluation of the acoustic field was done in water and through an *ex vivo* cut out and hollowed out nonhuman primate skull, of the species *macaca mulatta*. A coupling cone and a supporting frame for the skull were 3D printed to position the skull relative to the transducer and the lens during measurements (see Fig. 2).

B. Lens design and manufacturing

Holograms were calculated with time-reversal methods considering the boundary conditions used in the experimental validation, i.e., including the *ex vivo* skull and also

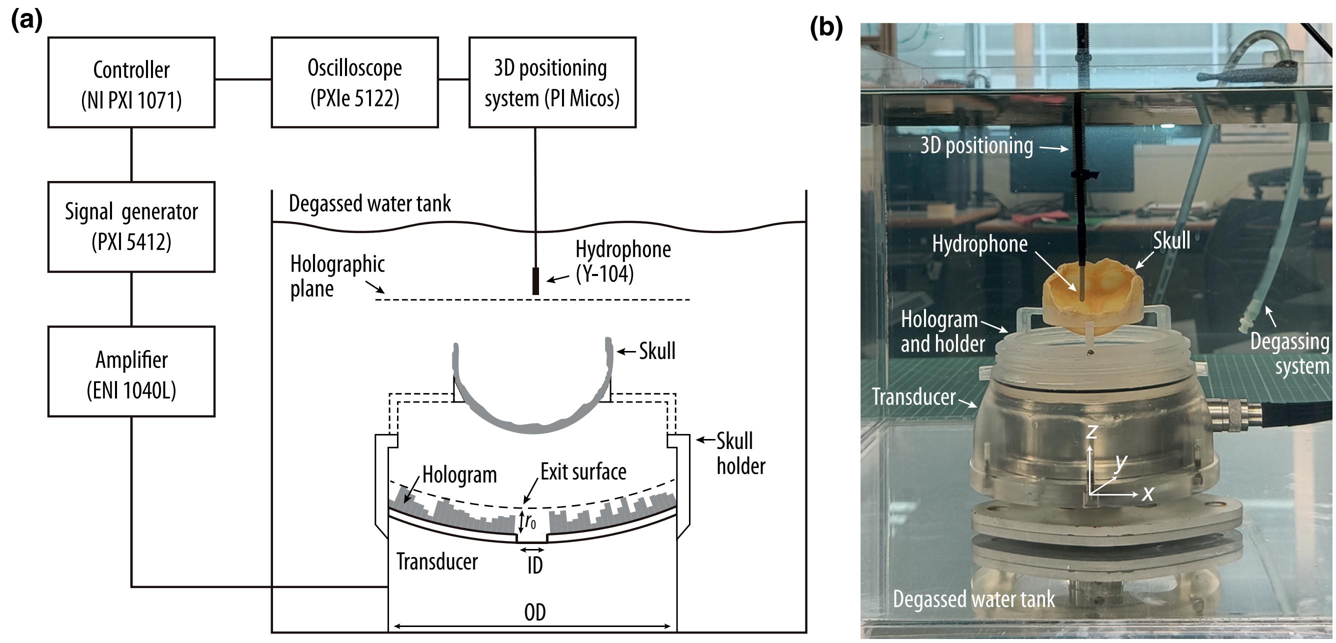

FIG. 2. (a) Schematic of the experimental setup. The transducer is driven with a signal generator using an amplifier. Each time a signal is emitted, a trigger is sent to the oscilloscope to capture the acoustic field with the hydrophone. Once the signal ends, the 3D positioning system moves the hydrophone to the next measurement position. (b) Photograph of the experimental setup showing the transducer with the lens, the skull holder, and the macaque skull. The hydrophone lies in a position used for direct measurements.

the coupling cone and the supporting frame, as described by Jiménez-Gambín *et al.* [29].

The time-reversal method employed consisted on locating virtual sources at the desired target and simulating their radiated field during long time to take account for several reflections. These acoustic signals were recorded in a spherical exit surface parallel to the transducer, at spherical coordinates $\mathbf{r}_0 = (\theta, \phi, R - r_0)$, i.e., the surface is located at a distance r_0 from the transducer surface [see Fig. 2(a)]. To perform temporal inversion, the field at the transducer frequency, $P(\mathbf{r}_0)$, was complex conjugated, $P^*(\mathbf{r}_0)$, and used to produce the lens. To design the lens we considered a uniform Cartesian grid projected on the curved holographic surface, so the height of each pixel in the lens is calculated in spherical coordinates $h(\mathbf{r}_0) = h(\theta, \phi)$, considering they vibrate longitudinally as an elastic resonator. All pixels of the lens are perpendicular to the radiating surface, presenting the shape of truncated pyramids. The complex frequency-dependent transmission coefficient of each pixel, measured at the exit surface is given by

$$T(\mathbf{r}_0) = \frac{2Z_n e^{-ik_0(r_0 - h)}}{2Z_n \cos(k_L h) + i(Z_n^2 + 1)\sin(k_L h)}, \tag{13}$$

where $Z_n = Z_L/Z_0$ is the normalized impedance, $Z_0 = \rho_0 c_0$, $k_0 = \omega/c_0$, c_0, ρ_0 and $Z_L = \rho_L c_L$, $k_L = \omega/c_L$, c_L, and ρ_L, are the acoustic impedance, wavenumber, sound speed, and density in water and in the lens material, respectively. The height of each pixel is obtained by interpolating the value of $h(\mathbf{r}_0)$ that makes $\arg[P^*(\mathbf{r}_0)] = \arg[T(\mathbf{r}_0)]$. As each pixel acts as an element in a phased array, ideally at the exit of the lens we retrieve a time-reversed version of the recorded acoustic field.

Each lens is implemented in the numerical model for validation and also 3D printed with stereolithography techniques (Form 3, Formlabs, USA) using the Clear photopolymer, whose density and sound speed values were experimentally obtained ($\rho_L = 1186$ kg/m^3 and $c_L = 2599$ m/s, respectively). Attenuation value was set to $\alpha_L = 3.4$ dB/(cm-MHz$^\gamma$) as reported in the literature for similar photopolymers [16,29].

C. Test cases

Two holographic lenses were designed and evaluated in this study: a first lens with which we wanted to create four equidistant foci across the skull (*four-foci lens*), and a second preclinical case where we aimed to target the left postcommissural putamen of a macaque (*preclinical lens*). *Ex vivo* macaque skull morphology and acoustic characteristics were derived from tomographic images acquired with a Toshiba Acquilion Prime TC scanner, with in-plane resolution of 0.245 mm and slice thickness of 1 mm. These X-ray attenuation values were converted into acoustic impedance data (density and sound speed) by using the linear empirical relationships obtained by Mast [51] adjusting the data from Schneider *et al.* [52], implemented in the software k-Wave [47].

Tomographic data were interpolated to an isotropic spatial step of $dh = \lambda_0/6$, where $\lambda_0 = c_0/f_0$ in water, which corresponds to $dh = 0.5$ mm, matching the numerical grid used in simulations. Average and maximum density and sound speed values were as follows: $\rho_{\text{avg}} = 1563$ kg/m^3, $\rho_{\text{max}} = 2542$ kg/m^3, $c_{\text{avg}} = 2191$ m/s, and $c_{\text{max}} = 3237$ m/s. Acoustic attenuation was taken into account for backward and forward propagation simulations for both designing and numerically validating the holographic lens. This physical magnitude was considered to be constant for all the skull and set to $\alpha = 9.6$ dB/(cm-MHz$^\gamma$), with $\gamma = 1.1$, according to Cobbold [53].

To create the four-foci lens, four virtual sources were located at the coordinates (x, y, z) (−5.6, 5.6, 63) mm for focus F_1, (−5.6, −5.6, 63) mm for focus F_2, (5.6, 5.6, 63) mm for focus F_3, and (5.6, −5.6, 63) mm for focus F_4. The preclinical lens was created by setting a virtual source in the middle of the target brain structure, the left post-commissural putamen of the specimen, that was identified in co-registered MRI images by an experienced neuroscientist, at coordinates (−6.6, −11.2, 55.3) mm. Each virtual source was set to emit sinusoidal continuous signals with the same phase and amplitude, and the resulting wavefront was recorded at the exit surface, located at $r_0 = 4$ mm in both cases.

Numerical validation of the acoustic field generated by each holographic lens was performed by considering the transducer was homogeneously vibrating, producing a 20-cycle sinusoidal pulsed-burst signal, with unitary amplitude. Maximum pressure in steady state was recorded, and its amplitude was scaled to the maximum pressure obtained experimentally using the angular spectrum projection.

D. Experimental procedure

All acoustic experiments were carried out in a tank of dimensions 400 × 800 × 600 mm^3, filled with degassed water at room temperature maintained by a water conditioning unit (WCU Series, Sonic Concepts, USA).

We used high-temperature water-insoluble coupling gel (Sonotech Sono 600) to ensure constant coupling of the lens to the transducer during experiments. The transducer was excited with a 20-cycle sinusoidal pulse burst at 500 kHz using a signal generator (model PXI-5412, 14-bit, 100 MS/s, National Instruments, USA) and amplified with a linear rf amplifier (model 1040L, 400 W, 55 dB, ENI, Rochester, NY, USA). Acoustic fields were measured with a piezoelectric hydrophone (model Y-104, −225.5 dB re 1 V/μPa at 1 MHz, Sonic Concepts, USA), calibrated from 40 kHz to 2 MHz, mounted on a 3D axis system (5-μm resolution, PI Micos GmbH, Germany). Lens, cone, and skull holder were 3D printed and mounted matching simulation conditions. The skull was located into its holder, which smoothly fitted on the design position. A schematic and a photograph of the experimental setup are presented in Fig. 2.

The origin of coordinates was set at the center of the hole of the transducer. Direct measurements of the four-foci lens were performed in two x-z planes ($-12.5 < x < 12.5$ mm, $47 < z < 72$ mm, at $y = -5.6$ mm and $y = 5.6$ mm, respectively), two y-z planes ($-12.5 < y < 12.5$ mm, $47 < z < 72$ mm, at $x = -5.6$ mm and $x = 5.6$ mm, respectively) and one x-y plane ($-12.5 < y < 12.5$ mm, $-12.5 < x < 12.5$ mm, at $z = 63$ mm). The 2D measurement for holographic projection was performed in a x-y plane of 35 × 30 mm^2 at $z = 72$ mm.

Direct measurements of the preclinical lens through the skull were performed in one x-z plane ($-14.5 < x < 1.5$ mm, $44 < z < 71$ mm, at $y = -11$ mm), one y-z plane ($-19.5 < y < -5.5$ mm, $44 < z < 71$ mm, at $x = -6.5$ mm) and one x-y plane ($-19.5 < y < -5.5$ mm, $-14.5 < x < 1.5$ mm, at $z = 55.5$ mm). The 2D measurement for holographic projection was performed in a x-y plane of 32 × 37 mm^2 ($-21.5 < x < 10.5$ mm, $-28 < y < 8.5$ mm) at $z = 71$ mm.

All measurements had a spatial resolution of 0.5 mm, matching the simulation resolution. Simulated and measured fields were spline interpolated to 0.1 mm precision for a more accurate calculation of location, sizes, and volumes of each focus. Volumes of each focus were calculated using an amplitude threshold of half the peak intensity.

In addition to transcranial measurements, projection methods were applied to estimate the acoustic pressure field at the exit surface of the lens. This was performed for both test cases in the water tank and in the absence of the skull. In this case, for each lens one x-y plane measurement was performed at $z = 44$ mm, and from −50 mm to 50 mm in both x and y directions, using a spatial resolution of 1 mm. To ensure that the exit plane of the lens and the plane measurement were completely parallel, transformations to its coordinates' system were performed as described by Kaloev *et al.* [54].

IV. RESULTS

A. Four-foci lens

Direct measurements for the four-foci lens show four clear focal spots, matching the design locations. By driving the transducer at 0.1 V, the peak pressure is 0.12 MPa at the focus F_2. Focus F_1, F_3, and F_4 present a peak pressure of 0.1, 0.08, and 0.09 MPa, respectively. Figures 3(a)–3(d) show the transverse field, $p(x, y)$, at $z = 63$ mm (at the location of the foci), obtained by forward simulation, projection using time reversal and angular spectrum, and direct measurements, respectively. Figures 3(e)–3(h) show the corresponding sagittal planes, $p(y, z)$, at $x = 5.6$ mm (at the location of the focus F_1). All the measuring methods provide similar results. In particular, the fields calculated using the projection techniques

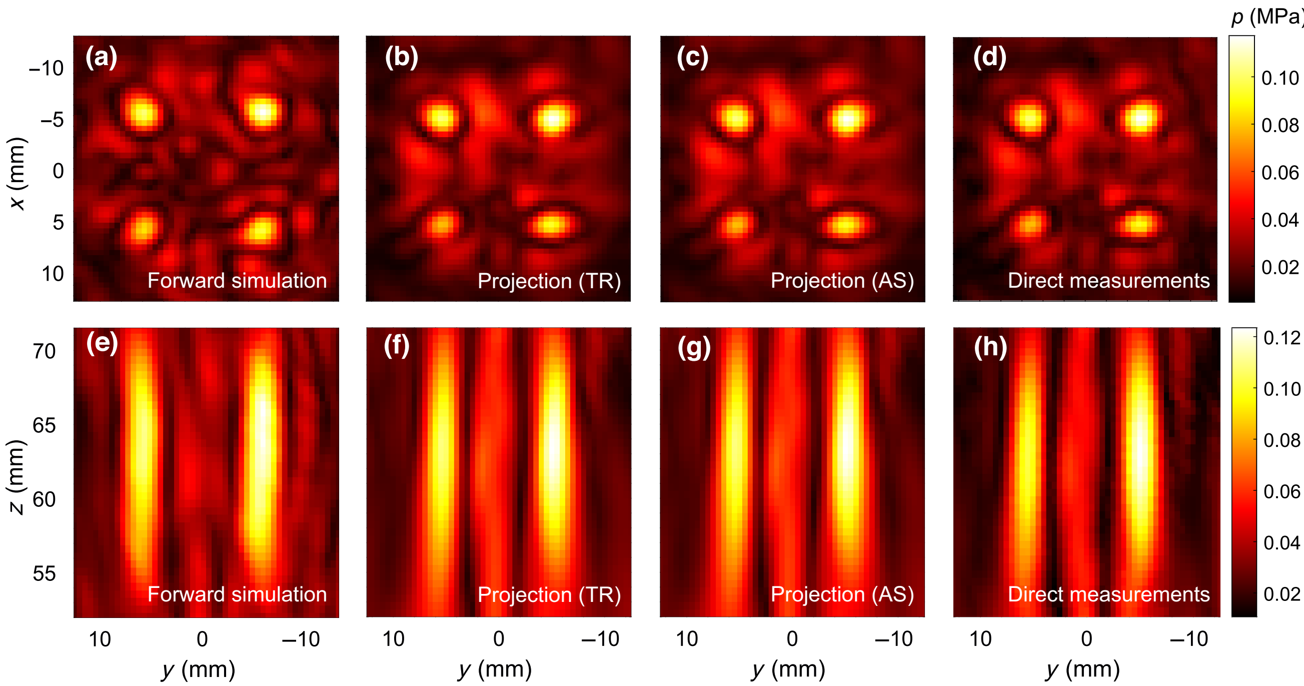

FIG. 3. Transverse field, $p(x,y)$, for the four-foci lens at $z = 63$ mm for (a) forward simulation, (b) time-reversal projection, (c) angular spectrum projection and (d) direct measurement. Axial field, $p(y,z)$, for (e) forward simulation, (f) time-reversal projection, (g) angular spectrum projection, and (h) direct measurements.

are almost identical, with differences well below $< 1\%$. Direct measurements also match the field obtained using both projection techniques. The maximum field difference between direct measurements and projections, and through the focal region (defined as the region from -8 to 8 mm in both x and y directions and from 52 to 17 mm in z) is 9.4%, with a mean difference value of 1.4%. Comparing the direct measurement at the x-y plane and the result of the time-reversal projection (from -8 to 8 mm in both x and y directions), we get that mean difference over this plane is 5.8% (5.9% when comparing with angular spectrum), where minimum differences are found in the foci region ($< 3\%$). Resemblances in terms of focal spot location and their lateral and axial dimension are summarized in Table I. The maximum difference in the peak pressure location is 1 mm in the z direction for the focus F_1 and between experiment and both projection techniques. Lateral dimensions of all four foci are similar between experiment and projections, with maximum differences of 0.2 mm. The maximum difference is found in the z direction, where there exist a discrepancy of 1.5 mm in the axial FWHM at the focus F_2.

Figure 4(a) shows a detailed field cross section over the four foci. Comparing experiment with simulation, there exist a discrepancy in the peak pressure location, which is evident at insets Figs. 4(b)–4(e). The maximum focal shift in the y direction appears for focus F_3, where a displacement of 2.3 mm is observed between forward simulation and direct measurements. In general, all foci in forward simulation appear further apart in x and y directions than in experiment and projection techniques.

Volumes were not characterized by direct measurements due to time and computational storage limitations. Instead, 3D fields were calculated by projecting the measured field using time-reversal or angular spectrum methods. In addition, forward simulations are inherently 3D. Figure 4(f) shows a 3D rendering of the forward simulated and projected fields, where isosurfaces are obtained by using a threshold of $I = I_{\max}/2$. Both projection methods results in a very similar 3D field. Using forward simulations, the volume corresponding to each focal spot, from F_1 to F_4, are 17.1, 21.6, 25.1, and 16.5 mm^3, respectively. For time-reversal projection, volumes are 18.7, 17.4, 21.8, and 13.4 mm^3, while for angular-spectrum projection these values are 18.2, 17.2, 21.1, and 13.4 mm^3, respectively.

B. Preclinical lens

For the preclinical lens, direct measurement presented a maximum pressure value of 0.13 MPa when driving the transducer at 0.1 V, while for both time-reversal and angular spectrum projection this value was of 0.126 MPa, and 0.128 MPa, respectively. Figures 5(a)–5(h) graphically compares x-y and y-z planes over the maximum for forward simulation, time-reversal and angular spectrum projection, and direct measurements. Over the focal region (defined as the region $-12 < x < -2$ mm, $-16.5 < y < -6.5$ mm, and $45 < z < 66$ mm), the mean-field difference

TABLE I. Results for the four-foci lens and the preclinical lens acoustic fields.

		Four-foci lens				
		Focus 1	**Focus 2**	**Focus 3**	**Focus 4**	**Preclinical focus**
Coordinates (mm)	Simulation	(−6.1,5.1, 64.5)	(−5.1, −5.1, 63.5)	(6.1, 6.1, 62.5)	(5.1, −6.1, 64.5)	(−7.1, −11.6, 55.9)
	Experiment	(−4.9, 5.2, 63)	(−4.9, −5.2, 63)	(5.1, 4.8, 62)	(5, −5.2, 63.5)	(−7.1, −11.5, 56)
	Time reversal	(−5, 5.2, 64)	(−5, −5.2, 63.5)	(5, 5.2, 62.5)	(5, −5.2, 63.5)	(−7.1, −11.5, 55.5)
	Angular spectrum	(−5, 5.2, 64)	(−5, −5.2, 63.5)	(5, 5.2, 63)	(5, −5.2, 63.5)	(−7.1, −11.5, 55.5)
Peak press. (MPa)	Simulation	0.103	0.119	0.078	0.093	0.131
	Experiment	0.101	0.117	0.077	0.091	0.131
	Time reversal	0.102	0.116	0.077	0.092	0.131
	Angular spectrum	0.103	0.119	0.078	0.093	0.131
FWHM-x (mm)	Simulation	3.2	3.1	3.0	3.5	3.1
	Experiment	3.0	3.1	3.1	2.5	5.3
	Time reversal	3.0	3.2	3.1	2.4	5.3
	Angular spectrum	3.0	3.1	3.0	2.4	5.2
FWHM-y (mm)	Simulation	3.1	2.9	3.2	2.9	3.2
	Experiment	3.1	3.4	3.2	3.6	4.3
	Time reversal	3.2	3.4	3.2	3.8	4.3
	Angular spectrum	3.2	3.4	3.1	3.8	4.3
FWHM-z (mm)	Simulation	16.7	15.5	15.9	16.6	16.5
	Experiment	···	17.2	17.5	16.1	···
	Time reversal	20.2	15.6	17.6	15.3	27.7
	Angular spectrum	21.3	15.9	17.3	15.3	27.6
Volume (mm^3)	Simulation	17.1	21.6	25.1	16.5	21.4
	Experiment	N/A	N/A	N/A	N/A	N/A
	Time reversal	18.7	17.4	21.8	13.4	91.0
	Angular spectrum	18.2	17.2	21.1	13.4	91.4

between the two projection techniques is 1.5%, while the maximum local difference is 22%. Comparing direct measurements at the x-y plane and time-reversal projection the mean-field difference is 10.6% (10.3% when comparing with angular spectrum). Table I shows several quantitative metrics, e.g., the location and amplitude of the acoustic focus, for the four techniques. Peak pressure location is very similar for both projection techniques, but between

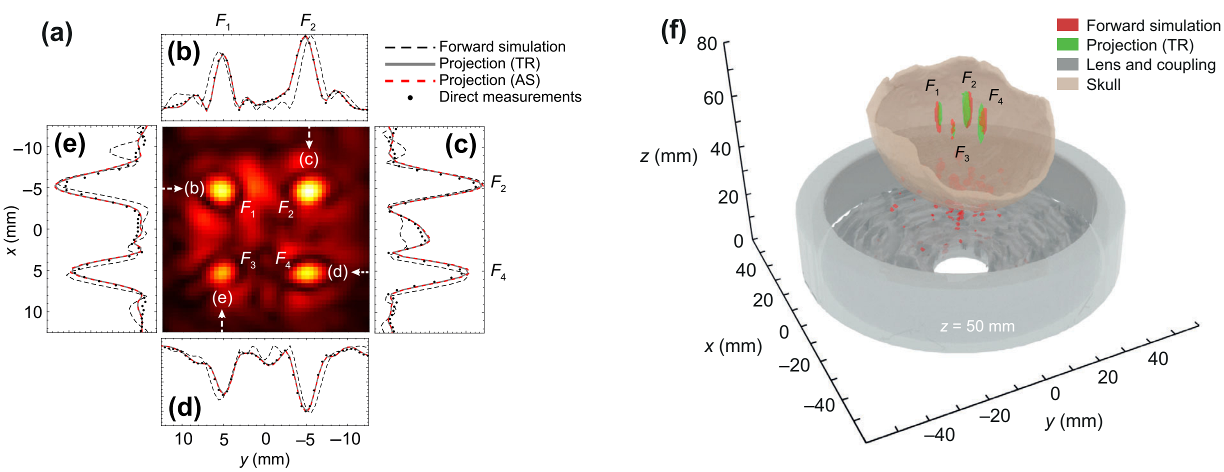

FIG. 4. (a) 2D plane at the peak pressure for the time-reversal field (at $z = 63$ mm) of the four-foci lens with linear cuts over each focus maximum for simulation, experiment, time reversal (TR), and angular spectrum (AS) over (b) y axis for F_1 and F_2 foci, (c) x axis for F_2 and F_4 foci, (d) y axis for F_3 and F_4 foci, and (e) x axis for F_1 and F_3 foci. (f) 3D representation of the simulated and time-reversed (TR) field of the four-foci lens and its location relative to the skull (multimedia view in the Supplemental Material [55]).

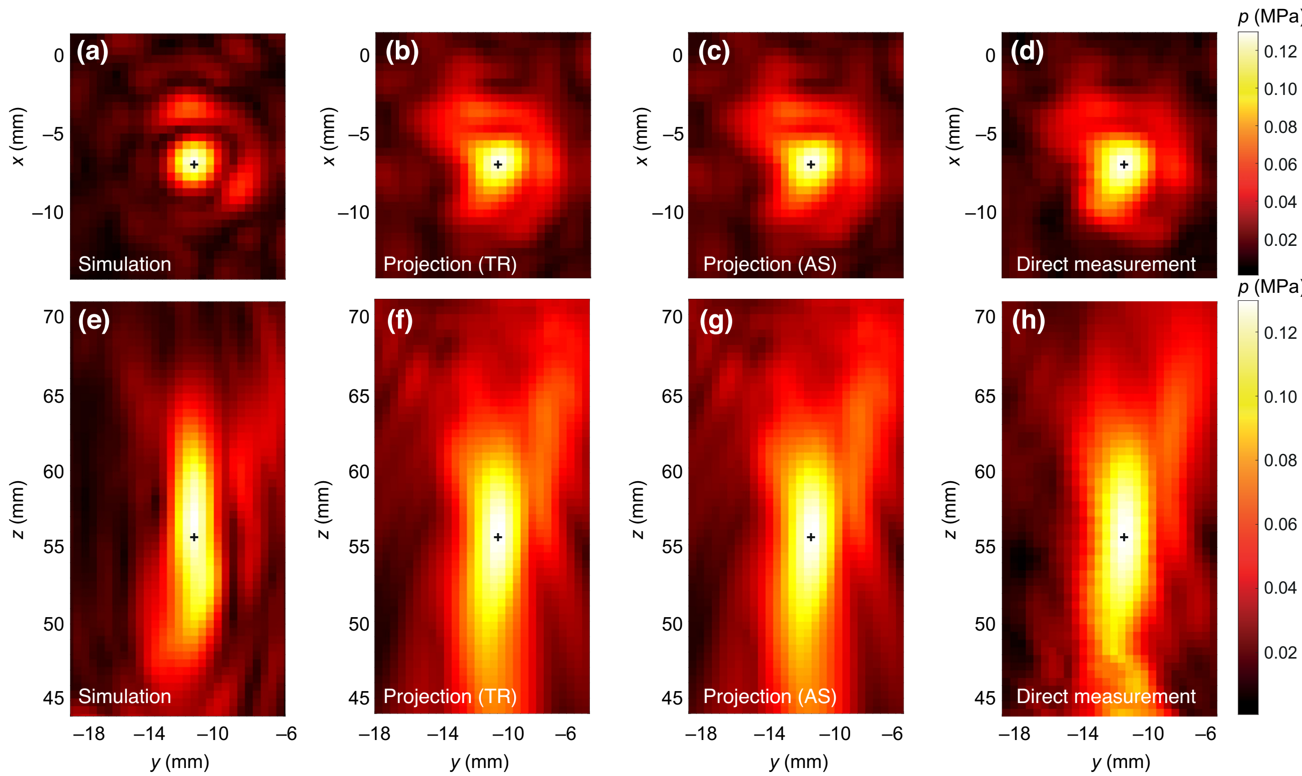

FIG. 5. Transverse field, $p(x, y)$, for the preclinical lens at $z = 63$ mm for (a) forward simulation, (b) time-reversal projection, (c) angular spectrum projection and (d) direct measurement. Axial field, $p(y, z)$, for (e) forward simulation, (f) time-reversal projection, (g) angular spectrum projection, and (h) direct measurements.

direct measurements and projection methods there exists a difference of 0.5 mm in the z direction. Lateral dimensions are similar between direct measurements and projection methods (see Table I). However, note that longitudinal dimension could not be estimated by direct measurements due to the proximity of the hydrophone to the skull, which introduced strong reflections. In this case, projection techniques allow reconstructing the acoustic field close to rigid boundaries. Indirect reconstruction strategies also avoid possible artefacts that may appear due to reflections with the measurement device.

Comparing experimental techniques with forward simulation, lateral and longitudinal dimensions of the focus show discrepancies. Figures 6(a)–6(c) show a detailed picture of the peak pressure along the three axis, respectively. While the FWHM obtained by time-reversed projection is $5.3 \times 4.3 \times 27.7$ mm^3, simulated field is $3.1 \times 3.2 \times 16.5$ mm^3. The 3D rendering shown in Fig. 6(d) compares the target structure, the reconstructed field by forward simulation, and the field reconstructed by TR projection method. The corresponding 3D volumes are 91.2 mm^3 for time-reversed projection, while 21.4 mm^3 for forward simulation. As the focus was designed to target the left postcommissural putamen, we have evaluated the volume of the target that was sonicated and the amount of energy that lied inside and out of the target structure. The target structure had a volume of 331.8 mm^3. The sonicated volume of the target, in simulation, was of 15.5 mm^3 , with 72.4% of the focus lying within the target. With projection, the sonicated volume of the target was of 30.3 mm^3, with 33.3% of the focus lying within the target.

C. Holographic lens characterization

In order to understand the obtained differences between simulation and experimental results, projection techniques were also applied to evaluate the acoustic field at the exit surface of the holographic lens. This was compared with the phase map obtained with simulation (also performing projection) and the phase map used to design the lens. The experimental field was backprojected from the measured plane to the curved lens exit surface (see Fig. 2). The simulated field was obtained by performing one simulation in the absence of the skull, recording all the signals at a plane located 44 mm above the transducer with lateral dimensions of 100×100 mm^2 to match the same experimental measurement plane, and performing a time-reversal simulation. For the sake of simplicity, we show only the preclinical lens.

Figures 7(a)–7(c) show the target, simulated, and experimental phase at the exit surface, respectively. We can

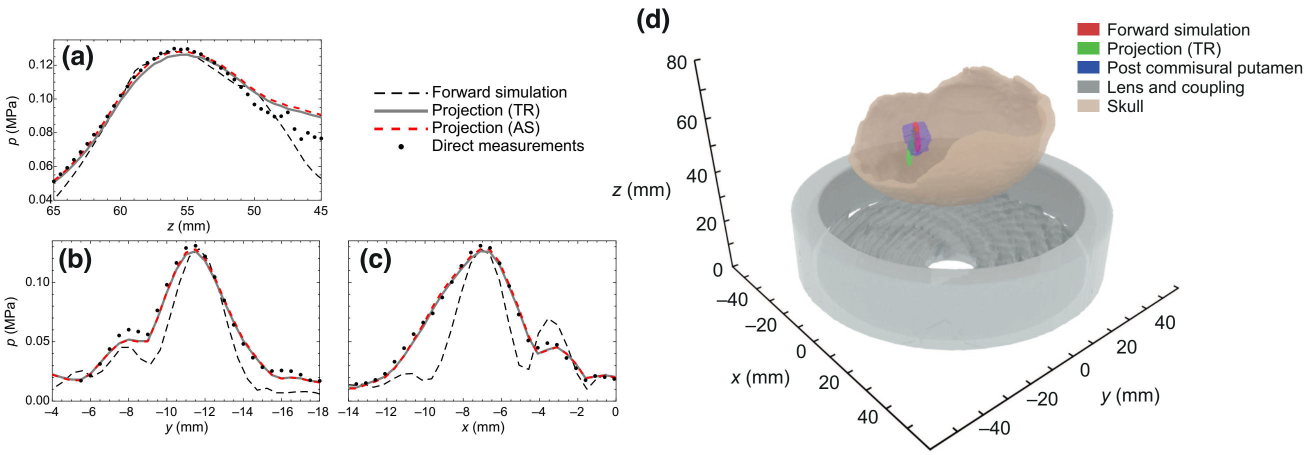

FIG. 6. Linear cuts of the preclinical lens acoustic pressure for simulation, time-reversal (TR) projection, angular spectrum (AS) projection, and direct measurements in (a) the z direction, (b) the y direction, and (c) the x direction. (d) 3D representation of the simulated and time-reversed (TR) field of the preclinical lens and its location relative to the skull and the postcomissural putamen (multimedia view in the Supplemental Material [56]).

observe concentric Fresnel rings in all phase maps indicating the focusing of the wavefront. However, the simulated and experimental phase map does not exactly match the target phase map at every location. These local errors, shown in Figs. 7(d) and 7(e), are larger at phase jumps and at the areas far from the focal spot, where Fresnel rings and its corresponding phase jumps are tighter. In this way, this analysis shows that the target phase is not perfectly encoded by the physical hologram design, with each pixel having a different height, as shown in the photograph, Fig. 7(g). The error between the target phase and the simulated phase map, Fig. 7(d), follows a normal distribution with mean value of 0.014 radians and standard deviation of 0.85 radians. Comparing the experimental and target phase, Fig. 7(e), the mean error is 0.012 radians and standard deviation of 0.85 radians. Finally, between the simulated phase and the experimental projection, Fig. 7(f), we find a difference with a mean value of 0.024 radians and standard deviation of 0.88 radians.

V. DISCUSSION

In this work, acoustic holography has been used to experimentally estimate the complex 3D acoustic fields produced by holographic lenses. By performing experimental measurements in a transverse plane, these methods can provide volumetric acoustic fields. The methods have been applied to estimate the field inside an *ex vivo* skull cap, opened in one side. Two different methods have been compared: time-reversal and angular spectrum projection. Projection methods have been compared with direct hydrophone measurements and forward simulations. Two test cases have been investigated: first, a holographic lens to create four equidistant foci through the skull and second, a holographic lens to focus on the left postcommissural putamen of the macaque.

For the four-foci lens case, we have first compared differences between both holographic techniques, observing that on the volume around the four foci the mean difference in pressure amplitude is 1.4%. When comparing with the 2D direct experimental measurement, this mean difference becomes 5.8%. Also, the peak pressure of the four foci appear at the same location and have very similar shape. The full width at half maximum in all three dimensions show errors smaller than 0.2 mm. The full potential of these projection techniques is unleashed when calculating the full 3D field by performing just one experimental measurement, i.e., a transverse 2D plane. This approach allows calculating metrics such as the treated volume. For example, for the four foci lens, volumes were 19.2 ± 0.3 mm^3 (focus F_1), 18.0 ± 0.1 mm^3 (focus F_2), 22.9 ± 0.4 mm^3 (focus F_3) and 14.4 ± 0.1 mm^3 (focus F_4). Using the proposed experimental system, the transverse 2D plane required for projections is composed of a total of 4331 waveforms (2.17 GBytes), every acquisition takes 3 sec on average (measuring, averaging, and moving to next position), leading to a total measurement time of 3.5 h. Note that to measure the whole 3D volume, i.e., $-12.5 < x < 12.5$ mm, $-12.5 < y < 12.5$ mm, and $47 < z < 72$ mm, with the same spatial resolution (0.5 mm), one must perform a total of 125 000 acquisitions, which would take 4.3 days. In terms of memory, the corresponding measurements would occupy 62.5 GBytes.

For the preclinical lens case, mean difference between both holographic techniques at the focus region is 1.5%, while comparing with the 2D direct experimental measurement, this mean difference becomes 10.6%. Also, the peak pressure of the focus appears at the same location and have very similar shape, where the average

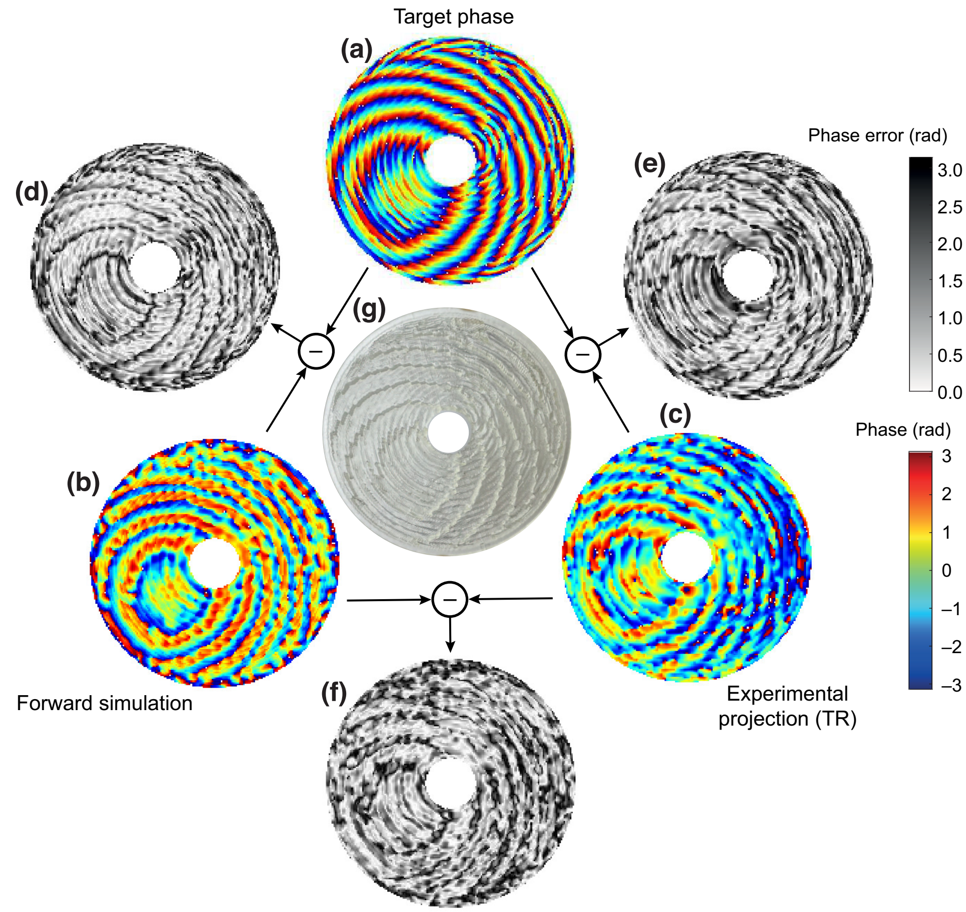

FIG. 7. (a) Recorded phase at the holographic plane for which the preclinical lens was designed. (b) Simulated phase after projection. (c) Experimental projected phase. (d) Difference between the goal and the simulated phases. (e) Difference between the goal and the experimental phases. (f) Difference between the simulated and the experimental phases. (g) Photo of the 3D-printed lens.

volume of the focus was 92.3 mm^3. Measurement time of the corresponding 2D transverse plane for projections (4736 measurements, 2.37 GBytes) is 4 h. In contrast, acquisition of direct measurements over the whole volume ($14 \times 14 \times 27$ mm^3) will lead to a total of 42 336 measurements, which would take 35.3 h (21.17 GBytes).

Greater differences are found between holographic projection and forward simulation for both lenses. For the four-foci lens, foci F_1 and F_3 appeared 1 mm apart in the x axis from the experimental location, and foci F_3 and F_4 had this same shift in the y axis. Also, forward simulation focus volumes are 17% greater than the experimental ones on average, except from the focus F_1 where it has been experimentally obtained that it was 6% larger. For the preclinical lens, experimentally the focus appears approximately at the same location than in the simulation, whereas experimentally determined volume was 75% greater than the simulated, with a region of relatively high pressure close to the skull. Discrepancies between simulation and experiment in both cases might be due to differences in the simulated skull properties, mode conversions in the skull, positioning errors and differences between the designed and the final 3D-printed lens.

While 3D direct measurements are feasible with modern acquisition systems, most hydrophones can vary their sensibility during time, in particular, polymer polyvinylidenfluorid (PVDF) ones are susceptible to changes during several hours of immersion. In addition, some hydrophones are very large to be introduced in cavities, such as a skull cap, limiting its use for transcranial measurements. In these situations, holographic projection can help to measure with large, sensitive and broadband devices, such as membrane hydrophones or large needle hydrophones. Another advantage of projection techniques is less exposure of the hydrophone to mechanical and thermal damage, including cavitation damage, since the field outside the focal point usually present a weaker amplitude than when the hydrophone is located directly at the focal spot. Also, holographic reconstruction makes it possible to characterize the field at the exit surface of a lens, identifying the error between the target phase to be encoded and the phase recovered by the manufactured lens.

However, the projection methods presented in this work are restricted to homogeneous media. Note the experiments were performed using a skull cap, rather than a full skull. In this sense, it will be difficult to estimate the field inside a closed cranial cavity by performing holographic projections. The time-reversal simulation strategy can be adapted to heterogeneous media by solving the constitutive equations considering spatially varying density, sound velocity, and sound-absorption maps. However, this would introduce uncertainties, as it requires precise knowledge of the properties of the medium and its location with respect to the holographic plane.

VI. CONCLUSIONS

In this work we have used holographic techniques, first, to create acoustic holographic lenses and, then, to evaluate their performance. In this way, time-reversal and angular spectrum projection methods were applied to obtain the whole volumetric field produced by an acoustic holographic lens focusing through an *ex vivo* macaque skull cap. Results show that projection methods are equivalent to direct measurements, whereas the former require only a single 2D-plane measurement. This strategy saves significant measurement time and memory requirements, especially when evaluating the complex field produced by acoustic holograms. Furthermore, this indirect procedure also mitigates signal artefacts that may appear during direct measurements due to the experimental setup. For example, in the studied cases we avoided bringing the hydrophone too close to the surface of the skull to avoid interferences due to bone-sensor reflections.

In addition, since phase-only holograms suffer from diffraction at the edges, corresponding with phase jumps at the central frequency, they cannot perfectly encode the target phase. Other sources of error, like tolerance of the 3D printing, positioning, coupling with the transducer, etc., also produce discrepancies between the target phase and the actual phase distribution generated by the lens. In this way, holographic reconstruction techniques emerge as a fundamental tool to experimentally recover the actual phase at the exit surface of the lens and compare it with the theoretical phase required for a particular design. This procedure can also help to design, tune, and test alternative hologram topologies to go beyond the limitations of current phase-only holograms, which is of great interest for low-cost therapeutical ultrasound systems and other emerging applications of acoustic holograms that involve the accurate synthesis of complex acoustic fields.

ACKNOWLEDGMENTS

This research has been supported by the Ministerio Español de Ciencia e Innovación and the Ministerio de Universidades through Grants Juan de la Cierva—Incorporación IJC2018-037897-I, Juan de la Cierva—Formación FJC2019-040453-I, Ramón y Cajal RYC2021-034920-I, Formación de Profesorado Universitario FPU19/00601. We are grateful for financial support from Agencia Estatal de Investigación (PID2019-111436RBC22 and PID2022-142719OB-C21 funded by MCIN/ AEI/10.13039/501100011033) and to the Agència Valenciana de la Innovació through Grants INNVA1/2022/37,INNVA2/2022/11 and METASMART Project INNEST/2022/345, and by Generalitat Valenciana through the programs Programa de Garantía Juvenil I+D EDGJID/2021/189, the Project of Ayudas Emergentes CIGE/2021/175, the Program Prometeo CIPROM/2021/003 and the Program Equipamiento e Infraestructuras FEDER 2021-22 IDIFEDER/2021/004. We acknowledge José Ángel Pineda-Pardo and CINAC (HM Hospital Puerta del Sur) for their support in providing us with the macaque *ex vivo* skull, TAC and MRI medical images and the postcomissural putament segmentation, and José Luis Alonso for technical support in the design of the experimental setup.

[1] D. Gabor, A new microscopic principle, Nature **161**, 777 (1948).

[2] A. F. Metherell, H. M. A. El-Sum, and L. Larmore, *Acoustical Holography* (Springer, New York, 1969), Vol. 1.

[3] F. L. Thurstone, Holographic imaging with ultrasound, J. Acoust. Soc. Am. **45**, 895 (1969).

[4] R. K. Mueller, Acoustic holography, Proc. IEEE **59**, 1319 (1971).

[5] E. G. Williams, J. D. Maynard, and E. Skudrzyk, Sound source reconstructions using a microphone array, J. Acoust. Soc. Am. **68**, 340 (1980).

[6] J. D. Maynard, E. G. Williams, and Y. Lee, Nearfield acoustic holography: I. Theory of generalized holography and the development of nah, J. Acoust. Soc. Am. **78**, 1395 (1985).

[7] W. Kreider, P. V. Yuldashev, O. A. Sapozhnikov, N. Farr, A. Partanen, M. R. Bailey, and V. A. Khokhlova, Characterization of a multi-element clinical HIFU system using acoustic holography and nonlinear modeling, IEEE Trans. Ultrason. Ferroelectr. Freq. Control **60**, 1683 (2013).

[8] O. A. Sapozhnikov, S. A. Tsysar, V. A. Khokhlova, and W. Kreider, Acoustic holography as a metrological tool for characterizing medical ultrasound sources and fields, J. Acoust. Soc. Am. **138**, 1515 (2015).

[9] IEC/TS62556, Ultrasonics—field characterization—specification and measurement of field parameters for high intensity therapeutic ultrasound (HITU) transducers and systems, (2014).

[10] B. Treeby, F. Lucka, E. Martin, and B. Cox, Equivalent-source acoustic holography for projecting measured ultrasound fields through complex media, IEEE Trans. Ultrason. Ferroelectr. Freq. Control **65**, 1857 (2018).

[11] Y. Li, X. Jiang, R.-q. Li, B. Liang, X.-y. Zou, L.-l. Yin, and J.-c. Cheng, Experimental realization of full control of reflected waves with subwavelength acoustic metasurfaces, Phys. Rev. Appl. **2**, 064002 (2014).

[12] Y. Zhu, J. Hu, X. Fan, J. Yang, B. Liang, X. Zhu, and J. Cheng, Fine manipulation of sound via lossy metamaterials with independent and arbitrary reflection amplitude and phase, Nat. Commun. **9**, 1632 (2018).

[13] M. D. Brown, Phase and amplitude modulation with acoustic holograms, Appl. Phys. Lett. **115**, 053701 (2019).

[14] M. Xu, W. S. Harley, Z. Ma, P. V. Lee, and D. J. Collins, Sound-speed modifying acoustic metasurfaces for acoustic holography, Adv. Mater. **35**, 2208002 (2023).

[15] Y. Hertzberg and G. Navon, Bypassing absorbing objects in focused ultrasound using computer generated holographic technique, Med. Phys. **38**, 6407 (2011).

[16] K. Melde, A. G. Mark, T. Qiu, and P. Fischer, Holograms for acoustics, Nature **537**, 518 (2016).

[17] M. D. Brown, J. Jaros, B. T. Cox, and B. E. Treeby, Control of broadband optically generated ultrasound pulses using binary amplitude holograms, J. Acoust. Soc. Am. **139**, 1637 (2016).

[18] M. D. Brown, B. T. Cox, and B. E. Treeby, Design of multi-frequency acoustic kinoforms, Appl. Phys. Lett. **111**, 244101 (2017).

[19] M. Brown, D. Nikitichev, B. Treeby, and B. Cox, Generating arbitrary ultrasound fields with tailored optoacoustic surface profiles, Appl. Phys. Lett. **110**, 094102 (2017).

[20] A. Marzo, S. A. Seah, B. W. Drinkwater, D. R. Sahoo, B. Long, and S. Subramanian, Holographic acoustic elements for manipulation of levitated objects, Nat. Commun. **6**, 1 (2015).

[21] S. Jiménez-Gambín, N. Jiménez, J. M. Benlloch, and F. Camarena, Generating bessel beams with broad depth-of-field by using phase-only acoustic holograms, Sci. Rep. **9**, 20104 (2019).

[22] N. Jiménez, J.-P. Groby, and V. Romero-García, Spiral sound-diffusing metasurfaces based on holographic vortices, Sci. Rep. **11**, 1 (2021).

[23] K. Melde, H. Kremer, M. Shi, S. Seneca, C. Frey, I. Platzman, C. Degel, D. Schmitt, B. Schölkopf, and P. Fischer, Compact holographic sound fields enable rapid one-step assembly of matter in 3D, Sci. Adv. **9**, eadf6182 (2023).

[24] Z. Ma, A. W. Holle, K. Melde, T. Qiu, K. Poeppel, V. M. Kadiri, and P. Fischer, Acoustic holographic cell patterning in a biocompatible hydrogel, Adv. Mater. **32**, 1904181 (2020).

[25] J. Kim, S. Kasoji, P. G. Durham, and P. A. Dayton, Acoustic holograms for directing arbitrary cavitation patterns, Appl. Phys. Lett. **118**, 051902 (2021).

[26] D. Andrés, J. Vappou, N. Jiménez, and F. Camarena, Thermal holographic patterns for ultrasound hyperthermia, Appl. Phys. Lett. **120**, 084102 (2022).

[27] D. Andrés, I. Rivens, P. Mouratidis, N. Jiménez, F. Camarena, and G. Ter Haar, Holographic focused ultrasound hyperthermia system for uniform simultaneous thermal exposure of multiple tumor spheroids, Cancers **15**, 2540 (2023).

[28] P. Kruizinga, P. van der Meulen, A. Fedjajevs, F. Mastik, G. Springeling, N. de Jong, J. G. Bosch, and G. Leus, Compressive 3D ultrasound imaging using a single sensor, Sci. Adv. **3**, e1701423 (2017).

[29] S. Jiménez-Gambín, N. Jiménez, J. M. Benlloch, and F. Camarena, Holograms to focus arbitrary ultrasonic fields through the skull, Phys. Rev. Appl. **12**, 014016 (2019).

[30] E. E. Konofagou, Y.-S. Tunga, J. Choia, T. Deffieuxa, B. Baseria, and F. Vlachosa, Ultrasound-induced blood-brain barrier opening, Curr. Pharm. Biotechnol. **13**, 1332 (2012).

[31] A. N. Pouliopoulos, S.-Y. Wu, M. T. Burgess, M. E. Karakatsani, H. A. Kamimura, and E. E. Konofagou, A clinical system for non-invasive blood–brain barrier opening using a neuronavigation-guided single-element focused ultrasound transducer, Ultrasound Med. Biol. **46**, 73 (2020).

[32] K. Hynynen, MRI-guided focused ultrasound treatments, Ultrasonics **50**, 221 (2010).

[33] A. Kyriakou, E. Neufeld, B. Werner, M. M. Paulides, G. Szekely, and N. Kuster, A review of numerical and experimental compensation techniques for skull-induced phase aberrations in transcranial focused ultrasound, Int. J. Hyperthermia **30**, 36 (2014).

[34] D. Coluccia, J. Fandino, L. Schwyzer, R. OÇť'orman, L. Remonda, J. Anon, E. Martin, and B. Werner, First noninvasive thermal ablation of a brain tumor with MR-guided focused ultrasound, J. Ther. Ultrasound **2**, 1 (2014).

[35] G. Maimbourg, A. Houdouin, T. Deffieux, M. Tanter, and J.-F. Aubry, 3D-printed adaptive acoustic lens as a disruptive technology for transcranial ultrasound therapy using single-element transducers, Phys. Med. Biol. **63**, 025026 (2018).

[36] D. Andrés, N. Jiménez, J. M. Benlloch, and F. Camarena, Numerical study of acoustic holograms for deep-brain targeting through the temporal bone window, Ultrasound Med. Biol. **48**, 872 (2022).

[37] S. Jiménez-Gambín, N. Jiménez, and F. Camarena, Transcranial focusing of ultrasonic vortices by acoustic holograms, Phys. Rev. Appl. **14**, 054070 (2020).

[38] S. Jiménez-Gambín, N. Jiménez, A. N. Pouliopoulos, J. M. Benlloch, E. E. Konofagou, and F. Camarena, Acoustic holograms for bilateral blood-brain barrier opening in a mouse model, IEEE Trans. Biomed. Eng. **69**, 1359 (2021).

[39] J. He, J. Wu, Y. Zhu, Y. Chen, M. Yuan, L. Zeng, and X. Ji, Multitarget transcranial ultrasound therapy in small animals based on phase-only acoustic holographic lens, IEEE Trans. Ultrason. Ferroelectr. Freq. Control **69**, 662 (2021).

[40] J. Seo, N. Koizumi, K. Yoshinaka, N. Sugita, A. Nomiya, Y. Homma, Y. Matsumoto, and M. Mitsuishi, Three-dimensional computer-controlled acoustic pressure scanning and quantification of focused ultrasound, IEEE Trans. Ultrason. Ferroelectr. Freq. Control **57**, 883 (2010).

[41] E. Martin, E. Z. Zhang, J. A. Guggenheim, P. C. Beard, and B. E. Treeby, Rapid spatial mapping of focused ultrasound fields using a planar Fabry–Pérot sensor, IEEE Trans. Ultrason. Ferroelectr. Freq. Control **64**, 1711 (2017).

[42] F. Thurstone, N. Kjosnes, and W. McKinney, Ultrasonic scanning of biologic tissue by a new technique, Science **149**, 302 (1965).

[43] A. R. Harland, J. N. Petzing, and J. R. Tyrer, Nonperturbing measurements of spatially distributed underwater acoustic fields using a scanning laser doppler vibrometer, J. Acoust. Soc. Am. **115**, 187 (2004).

[44] W. Moore and J. Bucaro, Measurement of acoustic fields using schlieren and holographic techniques, J. Acoust. Soc. Am. **63**, 60 (1978).

[45] K. Martin and R. Fernandez, A thermal beam-shape phantom for ultrasound physiotherapy transducers, Ultrasound Med. Biol. **23**, 1267 (1997).

[46] K. Melde, T. Qiu, and P. Fischer, Fast spatial scanning of 3D ultrasound fields via thermography, Appl. Phys. Lett. **113**, 133503 (2018).

[47] B. E. Treeby, B. T. Cox, k-Wave: MATLAB toolbox for the simulation and reconstruction of photoacoustic wave fields, J. Biomed. Opt. **15**, 021314 (2010).

[48] M. Fink, Time reversal of ultrasonic fields. I. Basic principles, IEEE Trans. Ultrason. Ferroelectr. Freq. Control **39**, 555 (1992).

[49] D.-L. Liu and R. C. Waag, Propagation and backpropagation for ultrasonic wavefront design, IEEE Trans. Ultrason. Ferroelectr. Freq. Control **44**, 1 (1997).

[50] X. Zeng and R. J. McGough, Evaluation of the angular spectrum approach for simulations of near-field pressures, J. Acoust. Soc. Am. **123**, 68 (2008).

[51] T. D. Mast, Empirical relationships between acoustic parameters in human soft tissues, Acoust. Res. Lett. Online **1**, 37 (2000).

[52] U. Schneider, E. Pedroni, and A. Lomax, The calibration of CT Hounsfield units for radiotherapy treatment planning, Phys. Med. Biol. **41**, 111 (1996).

[53] R. S. Cobbold, *Foundations of Biomedical Ultrasound* (Oxford University Press, New York, 2006).

[54] A. Kaloev, D. Nikolaev, V. Khokhlova, S. Tsysar, and O. Sapozhnikov, Spatial correction of an acoustic hologram for reconstructing surface vibrations of an axially symmetric ultrasound transducer, Acoust. Phys. **68**, 71 (2022).

[55] See Supplemental Material at http://link.aps.org/supplemental/10.1103/PhysRevApplied.20.044071 for a multimedia view of the four-foci lens acoustic field through the skull.

[56] See Supplemental Material at http://link.aps.org/supplemental/10.1103/PhysRevApplied.20.044071 for a multimedia view of the preclinical lens acoustic field through the skull.